



HAL
open science

Study of Residual Stresses in Additively Manufactured Ti-6Al-4V by Neutron Diffraction Measurements

David Gloaguen, Baptiste Girault, Bruno Courant, Pierre-Antoine Dubos, Marie-José Moya, François Edy, Joana Rebelo Kornmeier

► **To cite this version:**

David Gloaguen, Baptiste Girault, Bruno Courant, Pierre-Antoine Dubos, Marie-José Moya, et al.. Study of Residual Stresses in Additively Manufactured Ti-6Al-4V by Neutron Diffraction Measurements. Metallurgical and Materials Transactions A, 2020, 51 (2), pp.951-961. 10.1007/s11661-019-05538-w . hal-03409054

HAL Id: hal-03409054

<https://hal.science/hal-03409054>

Submitted on 16 Mar 2023

HAL is a multi-disciplinary open access archive for the deposit and dissemination of scientific research documents, whether they are published or not. The documents may come from teaching and research institutions in France or abroad, or from public or private research centers.

L'archive ouverte pluridisciplinaire **HAL**, est destinée au dépôt et à la diffusion de documents scientifiques de niveau recherche, publiés ou non, émanant des établissements d'enseignement et de recherche français ou étrangers, des laboratoires publics ou privés.

1 **Study of residual stresses in additively manufactured Ti-6Al-4V by neutron**
2 **diffraction measurements**

3
4 David GLOAGUEN^{1*}, Baptiste GIRAULT¹, Bruno COURANT¹, Pierre-Antoine DUBOS¹,
5 Marie-José MOYA¹, François EDY², Joana REBELO KORNMEIER³

6 ¹ Université de Nantes, Institut de Recherche en Génie Civil et Mécanique (UMR CNRS
7 6183), 58, rue Michel Ange - BP 420, 44606 Saint-Nazaire Cedex, France

8 ² IRT Jules Verne (French Institute in Research and Technology in Advanced Manufacturing),
9 Bouguenais, France

10 ³ Heinz Maier-Leibnitz Zentrum (MLZ), Technische Universität München, Garching,
11 Germany

12 * Corresponding author david.gloaguen@univ-nantes.fr

13
14 **Abstract:**

15 Neutron diffraction is a powerful non-destructive volumetric evaluation method for the
16 analysis of the internal stress state in components processed by Laser Powder Bed Fusion
17 (LPBF). High cooling rates and heterogeneous distribution of temperature during additive
18 manufacturing lead to large residual stress fields. Residual stresses developed during the
19 building process have unquestionably an important influence on the mechanical performance
20 and potentially lead to delamination from the support structures, shape distortion but also
21 crack formation. In the present work, neutron measurements have been carried out on cube-
22 shaped samples prepared by LPBF from a Ti-6Al-4V powder bed. A series of miscellaneous
23 positions (center, edge and corner) over 3 different depths (close substrate, middle and close
24 surface) have been analyzed by neutron diffraction so as to systematically characterize the full
25 stress tensor. The influence of shear stresses and second-order residual stresses on the stress
26 tensor analysis is also discussed in this work.

27
28 **Keywords:** Residual stress, Laser Powder Bed Fusion, Ti-6Al-4V, Neutron diffraction,
29 Additive manufacturing

1
2
3
4
5
6
7
8
9
10
11
12
13
14
15
16
17
18
19
20
21
22
23
24
25

1. Introduction

Additive Manufacturing (AM) techniques of metallic parts are expanding rapidly due to the technologic stake they represent: lightening of structure, complex architecture structure or reduced post-treatment processes [1]. Laser Powder Bed Fusion (LPBF) has a tremendous potential in AM methods because it enables to produce fully dense parts with desired inner structure and surface morphology [2]. LPBF technology can be used with various metallic powder materials such as Ti-6Al-4V [3,4], iron-based materials [5] and stainless steel [6]. Ti-6Al-4V is an alloy characterized by a combination of high strength, low-density and good corrosion resistance. Due to its biocompatibility, Ti-6Al-4V is ideal for medical applications and is also one of the main alloys used for high-temperature aerospace applications as a result of its high strength to weight ratio and good corrosion properties. Over the last decade, LPBF machines have become more and more popular in industrial settings which have led to extensive research regarding the potential use of LPBF for high added value functional Ti-6Al-4V parts production.

The high-temperature gradient, as a result of the locally concentrated energy input, can lead to property gradients arising from the different interdependent physical phenomena (metallurgical, thermal, mechanical and fluid mechanics aspects) occurring during this highly non-equilibrium process [6]. As a consequence, the LPBF process can result in residual stress gradients, likely large, and hence, crack formation and part deformations which have a significant effect on the macroscopic mechanical performance [7,8]. Therefore, it is an important issue to understand the development of residual stresses in LPBF processed components.

Internal stresses develop in built components due to the high cooling rates, the thermal gradients and the volumetric changes arising during phase transformations occurring during

1 the process [9]. Additionally, multiple process parameters have a significant influence on the
2 development of internal stresses. It has been notably shown that baseplate nature, power bed
3 preheating, powder characteristics, laser power, scanning speed, scanning strategy, number
4 and thickness of the successive layers and the geometry of the part for Ti-6Al-4V have a
5 significant impact on the residual stress set up [8,10]. Most of the process parameters
6 (typically scan speed and laser power) cannot be varied independently, as a fully dense part
7 always needs to be obtained. It is not necessarily easy to distinguish the influence of
8 individual process parameters on the internal stress generated during the process. In this
9 complex multi-parameter process, the investigation of the relationship set between LPBF
10 parameters values and residual stress formation is still necessary.

11 Although residual stresses are deeply studied for analogous processes such as multi-pass
12 welding, there are still too few experimental or/and numerical studies concerning the residual
13 stresses in components processed by LPBF [10].

14 Nevertheless, producing as-built parts of near full density and having mechanical properties
15 similar to those met for conventionally manufactured bulk materials (like casting or forging)
16 remains one of the most important goals of the AM community. The development of an in-
17 depth expertise of stress setup for AM materials is thus required to achieve such a goal,
18 especially if certification protocols need to be developed for AM components commissioning.
19 A major element of this process study involves the development of accurate and reliable
20 material property databases such as residual stress.

21 In most cases, residual macroscopic stresses are determined through a large variety of
22 methods which can be divided into two categories: destructive (contour method [11], hole
23 drilling [12], crack-compliance [13]) or non-destructive (e.g. X-ray and neutron diffraction
24 [6,14,15] methods). Each of those has drawbacks and benefits and varies in terms of probed
25 volume, accuracy or destruction level which can lead to a marked dispersion around results

1 reported in the literature. The most commonly used as non-destructive methods are X-Ray
2 (XRD) and Neutron Diffraction (ND), which permit, respectively, close surface (i.e. a few
3 tens of microns at best for conventional X-ray equipment) and volumetric residual stress
4 analysis in metallic materials [16]. Within this framework, ND is particularly relevant since
5 neutrons have a large penetration depth in most metallic alloys [6,17,18] up to cm length
6 scale, enabling non-destructive mapping of stress components through the full depth of an
7 AM part.

8 Nevertheless, two major drawbacks exist as regard to ND method for residual stress analysis.
9 The first one is the low acquisition rates of ND coupled with a long beam time acquisition.
10 The second is the extremely limited access to neutron sources. Furthermore, in order to
11 provide the full stress tensor defined by 6 independent components, although strain
12 measurement in 6 independent directions is mathematically sufficient, it is more suitable to
13 overdetermine the system by performing measurements in at least 12 directions to reduce the
14 related uncertainty [16]. In order to reduce the long measurement time due to the low
15 acquisition rates of ND, one strong assumption is commonly made so that the number of
16 measurement directions is reduced. It consists in assuming that the principal stress directions
17 are known and can be inferred from the sample geometry [6,16,19]. Strain measurements can
18 then be limited to these 3 (orthogonal) directions to resolve the principal stress components
19 σ_1 , σ_2 , σ_3 . For single track LPBF specimens, it seems to be reasonable to assume that the
20 principal stress, σ_1 , is along the scan track; σ_2 , lies in the perpendicular direction and σ_3 , lies
21 in the direction perpendicular to the baseplate (i.e. parallel to the plan formed by σ_1 and σ_2)
22 [6,15,20]. For more complex laser exposure strategies, this assumption is even less self-
23 evident and needs to be used carefully. If the shear stress components are not equal to zero,
24 the principal stress values determined with this assumption are simply wrong. As far as we

1 know, the determination of the full stress tensor has never been performed in Ti-6Al-4V parts
2 obtained by LPBF, whatever the laser exposure strategy used.

3 In the present work, ND measurements were carried out on cube-shaped samples
4 ($10\times 10\times 10\text{ mm}^3$) built by LPBF from a Ti-6Al-4V powder bed. A series of miscellaneous
5 positions (center, edge and corner) over 3 different depths (close substrate, middle and close
6 surface) have been analyzed. In order to obtain a substantial data set for strain analysis, 3
7 $\{hk.l\}$ reflections and 10 measurement directions for each reflection are probed at each
8 analyzed position, so as to systematically characterize the full strain tensor. Despite 6 strain
9 directions would have been sufficient to determine all the tensor components, data acquisition
10 has been fivefold increased enabling to check the reliability of the data and assess the
11 significance of shear stresses. In most of the studies, stress analysis by XRD or ND is only
12 performed with a single $\{hk.l\}$ reflection. The importance of second-order (or intergranular)
13 stresses is never quantified or even considered. A specific study is carried out in this paper to
14 investigate the importance of these stresses in samples prepared by LPBF.

15 **2. Experimental**

16 **2.1 Specimen preparation**

17 The parts used for this study were designed and built at the IRT Jules Verne (French Institute
18 in Research and Technology in Advanced Manufacturing, Bouguenais - France). Cube-shaped
19 specimens ($10\times 10\times 10\text{ mm}^3$) were produced using a SLM Solutions 280HL machine. They
20 were built from a Ti-6Al-4V powder (grade 23 ELI) with the following chemical
21 composition: Ti – balance, Al – 6 %, V – 4 %, Fe \leq 0.25 %, O \leq 0.13 %, H \leq 0.012 %,
22 C \leq 0.08 % and N \leq 0.05 % (weight %). The metallurgical characterization has been
23 presented in a previous study where more details concerning the analysis can be found [21].
24 Briefly, a SEM analysis of the powder has shown a mostly spherical grain morphology with

1 minimal satellites or smaller particles bonded to larger particles. An analysis of the powder
2 achieved by a laser scattering technique has showed a particle size distribution spread
3 between 20 and 63 μm with a median size of $d_{50} = 43 \mu\text{m}$. The LPBF process was optimized
4 to obtain an acceptable level of final part density. The final parameters used to manufacture
5 the specimens were: 30 μm -thick powder layers, a laser power of 175 W, a beam diameter of
6 80 μm , a scanning velocity of $775 \text{ mm}\cdot\text{s}^{-1}$ and a hatch spacing of 120 μm . The build plate was
7 made of the same Ti-6Al-4V alloy as the powder and was heated to a constant temperature of
8 200°C during the process. Concerning the scanning strategy, the starting point of the building
9 process is located on the edge of the part to be built. Each layer is then built through a back
10 and forth laser path with a rotation of 90° of the main laser path-vector between each layer.
11 SEM observations have revealed that a porosity density level of approximately 0.01 % is
12 obtained. Optical microscopy analysis showed the formation of fully columnar structures
13 along the LPBF building direction which is in accordance with the literature.

14 **2.2 Stress analysis by neutron diffraction**

15 First and foremost, it is worth to recall the stress analysis principles by diffraction and the
16 different associated assumptions [16]. The measured mean lattice strain $\langle \varepsilon(hk.l, \varphi, \psi) \rangle_{V_d}$ over
17 the diffracting volume V_d , for grains having the scattering vector Q (defined by inclination
18 and azimuth angles, respectively ψ and φ , as introduced in Figure 1) perpendicular to the
19 $\{hk.l\}$ planes, can be calculated from the measured lattice spacing $\langle d(hk.l, \varphi, \psi) \rangle_{V_d}$ and a
20 reference one $d_0(hk.l)$ using the following expression based on the true (rational) strain
21 definition [22]:

$$23 \quad \langle \varepsilon(hk.l, \varphi, \psi) \rangle_{V_d} = \ln \left(\frac{\langle d(hk.l, \varphi, \psi) \rangle_{V_d}}{d_0(hk.l)} \right) \quad (1)$$

24

1 Where $d_0(hk.l)$ is the strain-free lattice parameter related to the considered $\{hk.l\}$ reflection,
2 $\langle \rangle_{V_d}$ denotes an averaging over diffracting grains for the considered $\{hk.l\}$ plane family.

3 The lattice strain along the scattering vector can be calculated once 2θ angle has been
4 determined from measured diffraction peak using:

$$6 \quad \langle \varepsilon(hk.l, \varphi, \psi) \rangle_{V_d} = \ln \left(\frac{\sin \theta_0(hk.l)}{\sin \theta(hk.l, \varphi, \psi)} \right) \quad (2)$$

7
8 Where θ_0 is the Bragg angle regarding the stress-free material. The most appropriate solution
9 to determine this stress-free parameter in LPBF specimens consists in digging out this value
10 from a stress relaxed mini-cube ($2 \times 2 \times 2 \text{ mm}^3$), cut from twin specimens at the exact position
11 of the stress measurement (incorporating thus the metallurgical state of the measuring points).
12 The mini-cubes are then beam centered thanks to direct beam absorption measurements and a
13 theodolite device. Diffraction patterns are recorded while successively rotating around z and x
14 axes of the part coordinate system (x,y,z) (Figure 1). This results in an in-plane ((x,y) ; φ -scan
15 from 0 to 360° at $\psi = 0^\circ$) and out of plane (y,z) (ψ -scans from 0° to 90° at $\varphi = 0^\circ$) averaging
16 of the lattice spacing. [6, 23].

17 In order to resolve the macroscopic stress tensor σ , diffraction patterns have to be performed
18 along various directions (defined by ψ and φ angles). $\langle \varepsilon(hk.l, \varphi, \psi) \rangle_{V_d}$ values for those
19 directions can thereafter be used to calculate the stress tensor using the following relationship:

$$21 \quad \langle \varepsilon(hk.l, \varphi, \psi) \rangle_{V_d} = F_{ij}(hk.l, \varphi, \psi) \sigma_{ij} \quad (3)$$

22
23 $F_{ij}(hk.l, \varphi, \psi)$ are the diffraction stress factors for the considered $\{hk.l\}$ reflection [24]. These
24 factors can be calculated from material single-crystal elastic data and the Orientation

1 Distribution Function (ODF), thanks to an appropriate scale transition model. For
 2 macroscopically elastically anisotropic samples, it is important to specify that this relation
 3 remains valid. In equation (3), the second-order stresses (or intergranular stresses) are
 4 however neglected. The deviations of grain stresses from macroscopic stresses are then
 5 considered as exclusively resulting from elastic anisotropy. The deviations due to the
 6 anisotropy of the thermal expansion coefficients, plastic anisotropy or heterogeneity of phase
 7 transformation are not explicitly taken into account [25].

8 For quasi-isotropic materials having no preferential crystallographic orientation (i.e.
 9 elastically anisotropic grains in a randomly distributed crystallographic orientation sample),
 10 the correlation between the lattice strains obtained in measuring directions (φ, ψ) and the full
 11 stress tensor is simply given by:

12

$$\begin{aligned}
 13 \quad & \langle \varepsilon(hk.l, \varphi, \psi) \rangle_{V_d} = \\
 14 \quad & \frac{1}{2} S_2(hk.l) [\sigma_{11} \cos^2 \varphi + \sigma_{12} \sin 2\varphi + \sigma_{22} \sin^2 \varphi] \sin^2 \psi + \frac{1}{2} S_2(hk.l) [\sigma_{13} \cos \varphi \sin 2\psi + \\
 15 \quad & \sigma_{23} \sin \varphi \sin 2\psi + \sigma_{33} \cos^2 \varphi] + S_1(hk.l) [\sigma_{11} + \sigma_{22} + \sigma_{33}] \quad (4)
 \end{aligned}$$

16

17 $\frac{1}{2} S_2(hk.l)$ and $S_1(hk.l)$ are the well-known X-ray Elastic Constants (XEC) [16, 26]. They
 18 depend on the measured $\{hk.l\}$ reflection and take into account the elastic anisotropy of the
 19 grain.

20 If the principal stress coordinate system is known, only lattice strain measurements along
 21 these 3 orthogonal directions are required to determine the full stress tensor, which is diagonal
 22 in this case. The relation between the principal stress components σ_i and the principal strain
 23 components ε_i is then given by:

1

$$\sigma_i = \frac{(2S_1(hk.l) + \frac{1}{2}S_2(hk.l))}{\frac{1}{2}S_2(hk.l)(3S_1(hk.l) + \frac{1}{2}S_2(hk.l))} \varepsilon_i - \frac{S_1(hk.l)}{\frac{1}{2}S_2(hk.l)(3S_1(hk.l) + \frac{1}{2}S_2(hk.l))} \sum_j \varepsilon_j \quad j = 1,2,3 \quad j \neq i \quad (5)$$

3

4 For a polycrystal composed of elastically isotropic grains, the residual principal stresses are
5 simply calculated from the measured strains by the following relationship:

6

$$\sigma_i = \frac{E(1-\nu)}{(1+\nu)(1-2\nu)} \varepsilon_i + \frac{E\nu}{(1+\nu)(1-2\nu)} \sum_j \varepsilon_j \quad j = 1,2,3 \quad j \neq i \quad (6)$$

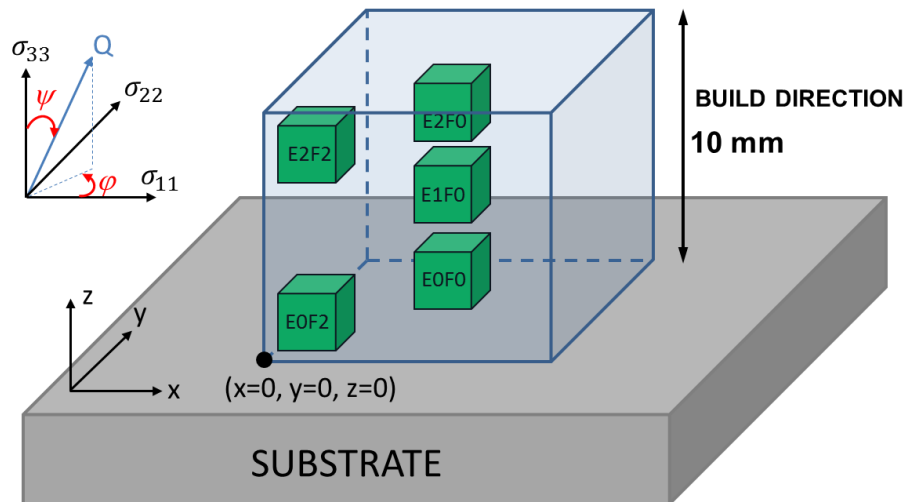
8

9 Where E and ν are, respectively, the Young's modulus and Poisson's ratio of the
10 polycrystalline aggregate.

11 Experiments have been performed at STRESS-SPEC beamline (Heinz Maier-Leibnitz
12 Zentrum – MLZ) [27] where one cube-shaped ($10 \times 10 \times 10 \text{ mm}^3$) baseplate-supported sample
13 has been analyzed. A monochromatic incident neutron wavelength of 1.55 \AA has been chosen
14 for the measurements. A χ goniometric assembly with a Position Sensitive Detector (^3He -
15 PSD) was used [28]. 3 reflections were studied: $\{10.3\}$ at $2\theta = 71.9^\circ$, $\{11.2\}$ at $2\theta = 77.9^\circ$ and
16 $\{20.1\}$ at $2\theta = 79.2^\circ$. The recording time for each ND measurement of a $\{hk.l\}$ peak took
17 around 60 min. Peak positions were determined by fitting the experimental data with a
18 Pseudo-Voigt function and a polynomial background.

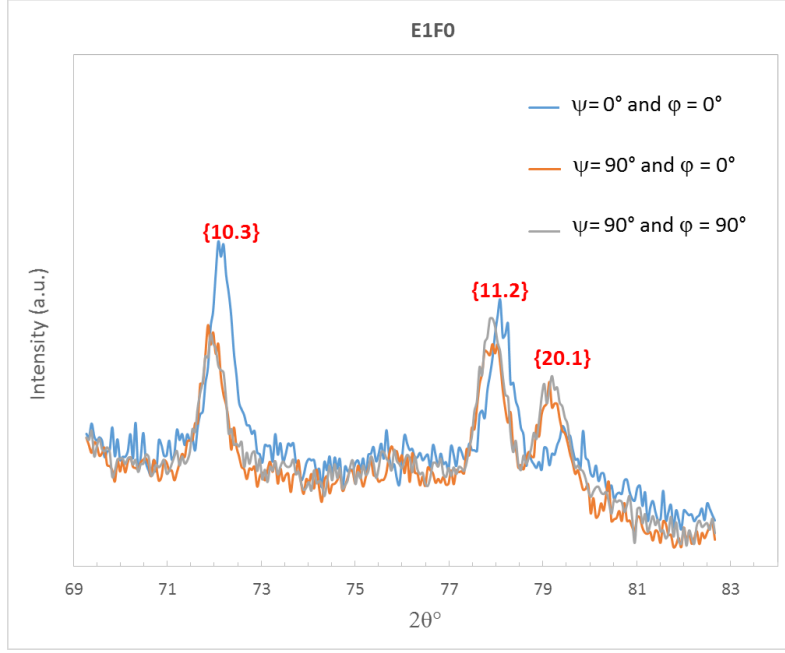
19 A series of miscellaneous positions (center, edge and corner) over 3 different depths (close
20 substrate, middle and close surface) has been probed by ND (Figure 1). Gauge volume has
21 been chosen as a compromise between acceptable measurement time scale and position

1 resolution in volume (i.e. $2 \times 2 \times 2 \text{ mm}^3$). Gauge position coordinates have integrated
 2 geometrical concerns ensuring the gauge to remain within the sample volume no matter the
 3 selected measurement direction, even for rim analyses. Five different gauge positions have
 4 been achieved (Figure 1) to analyze the residual stress distribution throughout the depth of the
 5 Ti alloy cube with a practicable testing time.



6
 7 Figure 1: schematic of the sample with measurement positions (in green) taken in the analysis.
 8 Note the coordinate system (x,y,z) where x and y directions are parallel to the baseplate and
 9 the z direction is the part building direction.

10 In order to obtain a consequent data set for strain analyses, 10 (φ, ψ) directions per diffraction
 11 peak have been probed on each of the 5 strain gauge positions: $(0^\circ, 0^\circ)$, $(0^\circ, 30^\circ)$, $(0, 60^\circ)$,
 12 $(0^\circ, 90^\circ)$, $(45^\circ, 30^\circ)$, $(45, 60^\circ)$, $(45^\circ, 90^\circ)$, $(90^\circ, 30^\circ)$, $(90, 60^\circ)$, $(90^\circ, 90^\circ)$. Figure 2 shows an
 13 example of ND patterns where diffraction intensities are plotted as function of the measured
 14 Bragg angle 2θ for the E1F0 measurement position. The differences in intensities of the
 15 different diffraction peaks for the (φ, ψ) directions point to the presence of a crystallographic
 16 texture in the LPBF part.



1

2 Figure 2: neutron diffraction patterns of the Ti-6Al-4V sample for different (ϕ, ψ) directions
 3 for the E1F0 measurement position. The diffraction peaks used in the study are also given.

4 The XEC have been calculated from single-crystal elastic constants ($c_{11} = c_{22} = 162.4$ GPa, c_{33}
 5 $= 180.7$ GPa, $c_{12} = 92$ GPa, $c_{13} = 69$ GPa and $c_{44} = 46.7$ GPa [29]) using an elastic-self
 6 consistent model [30]. For the calculation, we assume that the effect of crystallographic
 7 texture is low because the individual crystallites of the polycrystal are characterized by a low
 8 elastic anisotropy ($\frac{c_{11}+c_{12}-c_{33}}{c_{13}} = 1.07$, $\frac{c_{66}}{c_{44}} = 0.75$, $\frac{c_{11}+c_{12}+c_{33}}{4 c_{44}} = 1.07$ for titanium [31]). For
 9 the stress calculations, the quasi-isotropic assumption is used. The calculated XEC, $\frac{1}{2}S_2(hk.l)$
 10 and $S_1(hk.l)$, necessary for the stress calculation, are:

11 $\frac{1}{2}S_2(10.3) = 10.87 \cdot 10^{-6} \text{ MPa}^{-1}$, $S_1(10.3) = -2.58 \cdot 10^{-6} \text{ MPa}^{-1}$;

12 $\frac{1}{2}S_2(11.2) = 11.72 \cdot 10^{-6} \text{ MPa}^{-1}$, $S_1(11.2) = -2.88 \cdot 10^{-6} \text{ MPa}^{-1}$;

13 $\frac{1}{2}S_2(20.1) = 11.95 \cdot 10^{-6} \text{ MPa}^{-1}$, $S_1(20.1) = -2.96 \cdot 10^{-6} \text{ MPa}^{-1}$.

1 The full stress tensor is calculated according to the equation (4) for each measurement
2 position.

3

4

5 **3 Results and discussion**

6 3.1 Origin of the residual stresses in the LPBF process

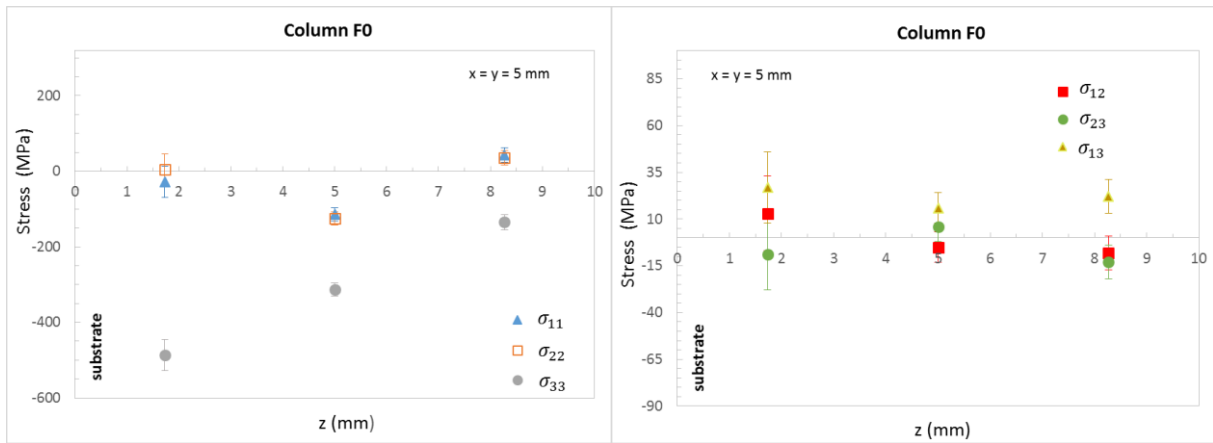
7 As a first step, it may be useful to recall the physical origins of the residual stresses being
8 built in this manufacturing process. LPBF is characterized by a complex thermal cycle. It is
9 defined by several phenomena: high heating and cooling rates, melt-back inducing the
10 simultaneous melting of the upper material layer (powder bed) and re-melting of underlying
11 previously solidified layers. The fast heating-cooling thermal cycles of LPBF associated with
12 volumetric changes, caused by both phase transformations and temperature gradients,
13 generate large residual stresses within LPBF parts.

14 Mercelis and Kruth [32] proposed a useful two-stage mechanism to explain how residual
15 stresses occur during the LPBF process: the Temperature Gradient Mechanism (TGM) and
16 the cool-down stage. The TGM enables describing the stress generation in a single melt track
17 while the cool-down mechanism depicts the behavior of an entirely melted powder layer. In
18 the TGM model, due to the fast warming of the top surface by the laser beam, the material
19 expands thermally. This thermal expansion of the heated top layer is restricted by the colder
20 underlying material. This phenomenon generates compressive stresses in the heat-affected
21 zone. Meanwhile, the material yield strength is reduced due to the temperature rise. If the
22 expansion is sufficiently significant, the compressive stress in the constrained solid material
23 exceeds the material yield strength and the top layer is then plastically compressed. During
24 the cooling, as a result of thermal contraction, a shrinkage of the top layers tends to occur.

1 The underlying material limits this deformation and elastic tensile strains are thus introduced
2 in the plastically deformed area which is balanced by a compressive zone below [33]. In the
3 framework of the cool-down model, the melted top layer initially has a higher temperature
4 than the underlying one. When the melt zone has cooled and solidified, the added top layer
5 shrinks owing to thermal contraction. This deformation is inhibited by the surrounding colder
6 material. Therefore, tensile stresses appear in the newly solidified upper layer and they are
7 balanced by compressive stresses in the underlying layers. Although these two models clearly
8 describe the major mechanisms involved in the residual stress generation during LPBF, the
9 stress field is naturally much more complex since the number of layers, the heat source path
10 pattern and the heat transfer are tremendously intricate [34].

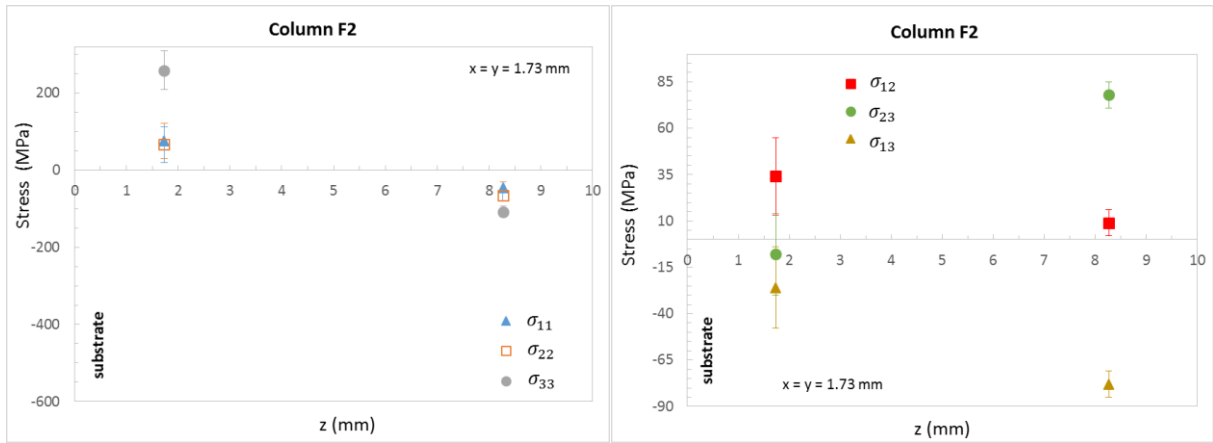
11 3.2 Evolution of stress components of the full stress tensor

12 Figures 3.a and 3.b show the evolution of stress components of the full stress tensor at 3
13 building heights ($z = 1.73, 5.00, 8.27$ mm) in the core sample i.e. central column F0
14 ($x = y = 5$ mm), coordinates matching the center of each probed volume. Let us first focus on
15 the development of the σ_{33} component for the central column F0 (Figure 3.a). Large negative
16 stress ($\sigma_{33} = -487 \pm 41$ MPa) at low z values (near the baseplate) decreasing with higher z
17 values (the minimum stress is found at $z = 8.27$ mm: $\sigma_{33} = -135 \pm 20$ MPa) is observed in
18 measurements. At this point, it must be reminded that the gauge volume ($2 \times 2 \times 2$ mm³) probed
19 in neutron experiments is large as compared to the thickness of the melted layers. The sample,
20 built with 30 μ m layer thickness, results in 67 layers per probed volume so it means that the
21 stresses are averaged over a large number of layers. Thus, it must be kept in mind that the
22 results obtained by ND indicate an average stress value and not an extremum value.



1
2
3

(a) (b)



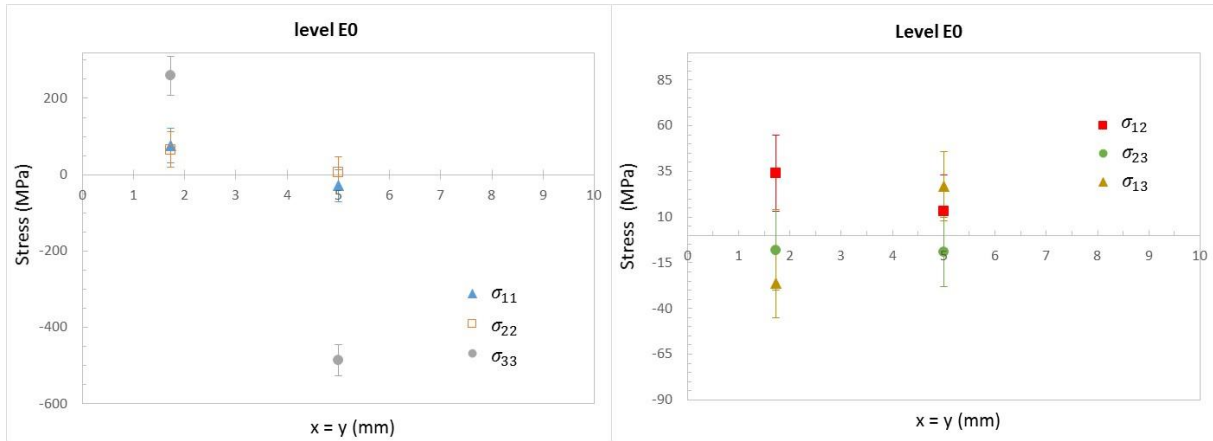
4
5

(c) (d)

6 Figure 3: residual stresses obtained by ND at several building heights in the central column
7 F0, i.e. core sample (a and b) and the column F2 (c and d) close to a corner of the analyzed
8 cube.

9 The stress value obtained at $z = 8.27$ mm is the mean stress obtained for a depth varying from
10 6.54 up to 10 mm and not the close-surface stress value. The residual stress increases rapidly
11 toward low compressive values as the top surface is approached. The normal stress could thus
12 even reach positive values at the subsurface. The heat transfer is actually weak along the
13 building direction, leading to a high-temperature gradient, bringing up tensile σ_{33} stress in the
14 upper section and compressive stress in the bottom section i.e. in the nearest region of the

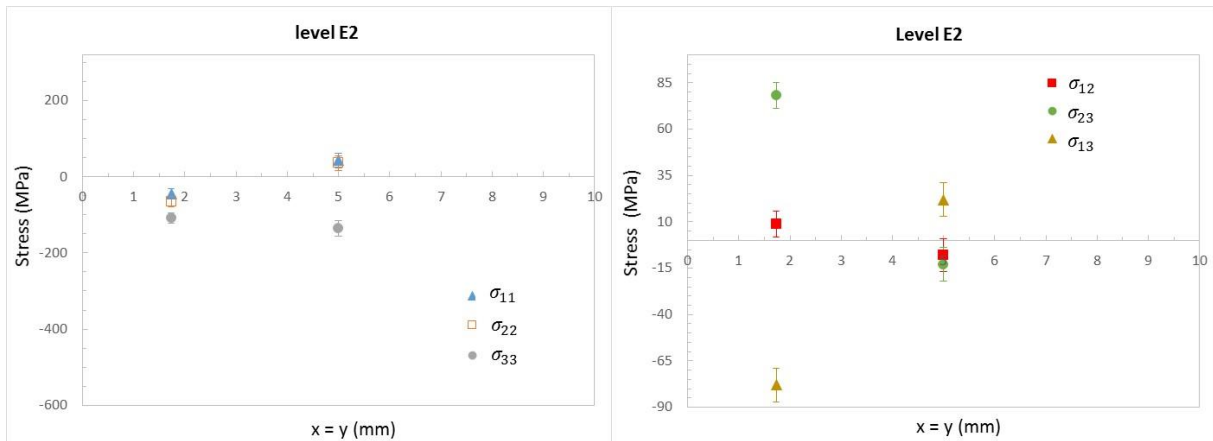
1 baseplate. The stresses along the building direction correspond to the process described above
 2 by the cool-down mechanism. Lower longitudinal (σ_{11}) and transversal (σ_{22}) stress level were
 3 present along the sample height which turned into tension ($\sigma_{11} = 43 \pm 19$ MPa) in the upper
 4 region. The laser scanning strategy, for which the laser path direction is alternated between
 5 each layer [$0^\circ/90^\circ$], tends to provide a homogeneous stress field in the x-y plane (Figure 4).



6

7 (a)

(b)



8

9 (c)

(d)

10 Figure 4: residual stresses obtained by ND at several building levels: close substrate (E1: a
 11 and b) and close surface (E2: c and d).

12 According to the residual stress analysis presented by Ali *et al.* [35], increasing powder bed
 13 pre-heating temperatures results in a lowering of residual stress due to a reduction in

1 temperature gradients during the LPBF process. On the other hand, components that remain
2 attached to the baseplate contain stress levels close to the material yield strength value
3 without preheating [36]. The mechanical properties of the specimen at ambient temperature
4 have been characterized by monotonic tensile tests: $R_E = 985 \pm 12$ MPa (yield strength) and
5 $\sigma_{UTS} = 1098 \pm 16$ MPa (ultimate tensile strength). In our study, stress magnitude is smaller
6 than the yield strength of the samples close to the baseplate in agreement with [35]. The stress
7 component $\sigma_{33} = -487 \pm 41$ MPa (column F0, $x = y = 5$ mm) gains on 50 % of the yield
8 strength.

9 Figure 3.b illustrates the distributions of shear stress components ($\sigma_{13}, \sigma_{23}, \sigma_{12}$) in the central
10 column F0. The shear stresses vary from -13 ± 9 MPa to 27 ± 19 MPa along the building
11 direction.

12 In the column F2 ($x = y = 1.73$ mm), near a corner of the cube, the residual stress state is quite
13 different from the previous case, especially for the normal stress component σ_{33} (Figure 3.c).
14 The stress magnitudes are lower due to the influence of the larger free surface with values
15 ranging from $\sigma_{33} = 259 \pm 50$ MPa ($z = 1.73$ mm) to $\sigma_{33} = -108 \pm 14$ MPa ($z = 8.27$ mm).
16 The sample shows an in-plane equi-biaxial stress state no matter the analyzed height.
17 Longitudinal and transversal stress values are ranging from 76 ± 46 MPa to $-66 \pm$
18 14 MPa (Figure 3.c). As can be seen, tensile stresses develop at low z values (near the
19 baseplate) while stresses turn into compression (slightly) with increasing z values. The highest
20 shear stress values are obtained in the column F2 (Figure 3.d) with values varying between
21 78 ± 7 MPa and -78 ± 7 MPa. In summary, the stress distribution near the surfaces tends
22 to have a lower compressive magnitude, even reaching tension mechanical stress state,
23 especially close to the baseplate at the cube corners (Figures 3.c and 4.a). This is in agreement
24 with previous works which showed that the bottom and top surfaces of LPBF specimens tend

1 to be in tension or low compression while the internal volume of the part being in
2 compression [32, 37].

3 3.3 The effect of assuming the principal directions in ND measurements for stress analysis

4 As mentioned in the introductory chapter, in most previous studies, one strong assumption is
5 usually made in order to reduce the number of measurement directions and thus the
6 experiment duration (related to the low acquisition rate of ND technique). Latter entails
7 assuming that the principal stress coordinate system is known and can be inferred from the
8 sample geometry. Strains can consequently be measured in only these 3 (orthogonal)
9 directions to determine the principal stresses $\sigma_1, \sigma_2, \sigma_3$. This stress state assumption is not a
10 true representation of the stress within the part, meaning that the use of equation (5) or (6)
11 may not provide the correct stress values. To highlight this problem, Table 1 shows the
12 evolution of the principal stress components σ_i , calculated from the equation (5), compared
13 to the results obtained for the normal components σ_{ii} with the relation (4) for the column F2.
14 The 3 principal stress components σ_i have been determined from the equation (5) with the
15 experimental lattice strain values measured at (φ, ψ) equal to $(0^\circ, 0^\circ)$, $(0^\circ, 90^\circ)$ and $(90^\circ, 90^\circ)$
16 for either each $\{hk.l\}$ reflection or combining the 3 reflections simultaneously. For the second
17 principal stress calculation method (reflection combination), since lattice strains were
18 determined in 3 different sample directions per diffraction peak, we obtain 9 linear equations
19 with 3 unknowns, to which we applied a least-squares procedure to determine the best
20 possible values for the 3 (unknown) principal stress components σ_i . Finally, it should be
21 underlined that there is no way to estimate the errors for the principal stress components when
22 only 3 directions are used in stress analysis for a single reflection.

23 The principal stress values calculated with the relation (5) are different from the previous case
24 (full stress tensor). The largest discrepancy is observed at $z = 1.73$ mm (E0F2). For example,

1 the normal stress value along the x-direction (Figure 1) varies in a significant way according
2 to the reflection selected in the stress analysis: $\sigma_1 \{10.3\} = 202$ MPa, $\sigma_1 \{11.2\} = 27$ MPa
3 and $\sigma_1 \{20.1\} = -291$ MPa. These results are quite different from those obtained previously
4 with equation (4): $\sigma_{11} = 76 \pm 46$ MPa. The largest difference is observed for the $\{20.1\}$
5 reflection. This discordance could be partly attributed to the poor quality of the diffraction
6 peaks for this reflection as regard to the low peak-to-background ratio (see Figure 2). The
7 same trend is observed for the other diagonal tensor component values σ_2 and σ_3 . However,
8 at $z = 8.27$ mm (E2F2), the calculated σ_i values are close to the σ_{ii} values determined for the
9 full stress tensor regardless the reflection or their combination.

Stress component	Assumption	E0F2	E2F2
σ_1 (MPa)	Principal stress- $\{10.3\}$	202	-46
	Principal stress- $\{11.2\}$	27	-37
	Principal stress- $\{20.1\}$	-291	-69
	Principal stress $\{10.3\}+\{21.1\}+\{20.1\}$	-16 ± 135	-51 ± 16
	σ_{11} -full stress tensor	76 ± 46	-45 ± 14
σ_2 (MPa)	Principal stress- $\{10.3\}$	166	-74
	Principal stress- $\{11.2\}$	18	-51
	Principal stress- $\{20.1\}$	-277	-91
	Principal stress $\{10.3\}+\{21.1\}+\{20.1\}$	-25 ± 135	-72 ± 16
	σ_{22} -full stress tensor	66 ± 46	-66 ± 14
σ_3 (MPa)	Principal stress- $\{10.3\}$	376	-137
	Principal stress- $\{11.2\}$	166	-84
	Principal stress- $\{20.1\}$	-354	-112
	Principal stress $\{10.3\}+\{21.1\}+\{20.1\}$	62 ± 135	-110 ± 16
	σ_{33} -full stress tensor	259 ± 50	-108 ± 14

10 Table 1: evolution of the principal stress components σ_i , calculated from equation (5), for
11 different $\{hk.l\}$ reflections and compared to the results obtained for the normal components
12 σ_{ii} , obtained with the relation (4), along the column F2.

13 At this point, the difference between the normal stress, determined from equation (4), and the
14 principal stress, obtained by equation (5), must be explained [38,39]. From the equation (4)

1 which permits to calculate the full stress tensor, one can easily notice that the relation shows
 2 no coupling between both shear and normal stresses and strains as soon as 3 orthogonal lattice
 3 strains along the macroscopic coordinate axes are measured (i.e. (φ, ψ) equal to $(0^\circ, 0^\circ)$,
 4 $(0^\circ, 90^\circ)$ and $(90^\circ, 90^\circ)$):

$$5 \quad \langle \varepsilon(hk.l, 0, 90) \rangle_{V_d} = \varepsilon_{11} = \frac{1}{2} S_2(hk.l) \sigma_{11} + S_1(hk.l) [\sigma_{11} + \sigma_{22} + \sigma_{33}] \quad (7)$$

$$6 \quad \langle \varepsilon(hk.l, 90, 90) \rangle_{V_d} = \varepsilon_{22} = \frac{1}{2} S_2(hk.l) \sigma_{22} + S_1(hk.l) [\sigma_{11} + \sigma_{22} + \sigma_{33}] \quad (8)$$

$$7 \quad \langle \varepsilon(hk.l, 0, 0) \rangle_{V_d} = \varepsilon_{33} = \frac{1}{2} S_2(hk.l) \sigma_{33} + S_1(hk.l) [\sigma_{11} + \sigma_{22} + \sigma_{33}] \quad (9)$$

8 If the sample geometry coordinate system coincides with the principal stress coordinate
 9 system, the shear strain components are equal to 0 and the principal strains ε_i correspond to
 10 normal strains ε_{ii} . The principal strains ε_i can be determined by measuring lattice strains
 11 along the macroscopic coordinate axes and the principal stresses are calculated using
 12 equations 7, 8 and 9.

13 If the shear stress components have non-zero values, the principal stresses are not defined
 14 along the 3 sample coordinate axes but they are in other directions depending on the shear
 15 strain values. The assumption claiming that the sample geometry coordinate system does
 16 overlay the principle stress coordinate system is then wrong. The principal stresses may,
 17 therefore, be much larger depending on the magnitude of the shear strains. Since the normal
 18 stress components σ_{ii} do not depend on the values of the shear strains (equations 7, 8 and 9),
 19 the stress components σ_{11} , σ_{22} , and σ_{33} are always true but not necessarily equal to the
 20 principal stresses σ_1 , σ_2 , and σ_3 . In other words, the normal stress components in any three
 21 orthogonal directions may be correctly calculated by measuring the strains in these three
 22 directions whether or not they are the principal directions. This is always verified because the

1 shear stress components do not affect the normal strains in a macroscopic isotropic material
 2 [39].

3 Through the diagonalization of the full stress tensor [38], it is possible to determinate the
 4 deviation of the principal stress directions (denoted (X,Y,Z)) from the LPBF part orthogonal
 5 axes (x,y,z) (defined in Figure 1) for each measurement point. Table 2 illustrates the angles
 6 between the principal stress directions and the specimen orthogonal stress directions.

Measurement position	Angle between x and X (in degree)	Angle between y and Y (in degree)	Angle between z and Z (in degree)
E0F0	19°	19°	4°
E0F2	137°	41°	9°
E1F0	19°	18°	5°
E2F0	34°	33°	8°
E2F2	51°	42°	40°

7 Table 2: angles between the principal stress directions (X,Y,Z) and the specimen orthogonal
 8 stress directions (x,y,z) for the different measurement positions.

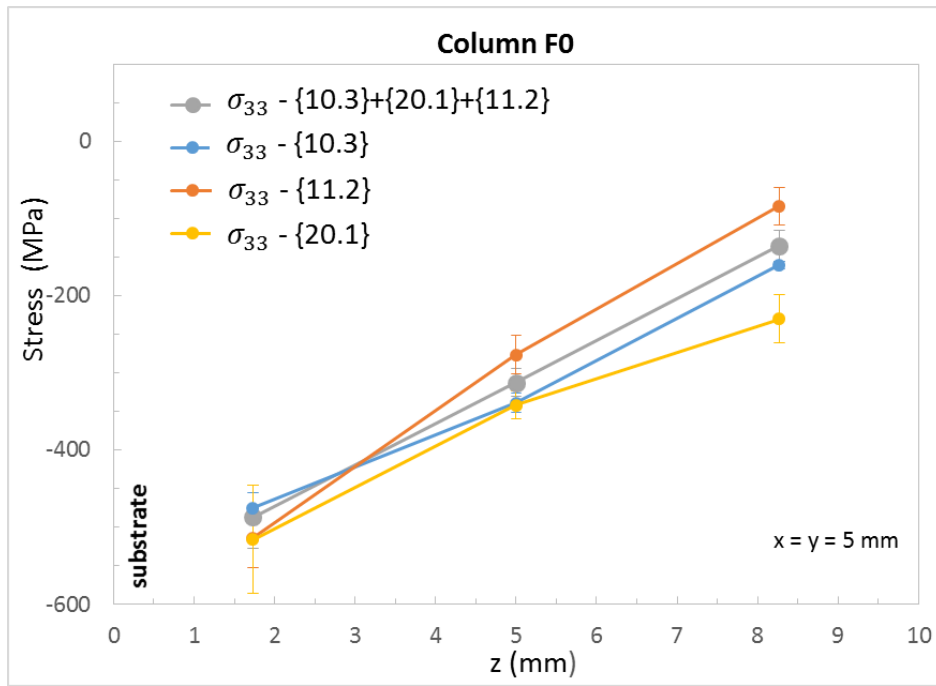
9 In the central column, for the E0F0 and E1F0 measurements positions, the principal directions
 10 were aligned with the sample axes within approximately 20 degrees. The principal stress
 11 values were within ± 4 MPa of the corresponding orthogonal stress values shown in Figure
 12 3.a. Near a corner of the cube (E0F2 and E2F2) or close to the top surface (E2F0), a large
 13 deviation is observed. This phenomenon is probably due to the influence of the free surface
 14 with a different thermal history of the probed region as compared to the internal volume of the
 15 part. The principal stress values are quite different from the normal stress component values.
 16 For example, at $z = 8.27$ mm (E2F2), the principal stress values (respectively the normal
 17 stress values) are: $\sigma_1 = 27$ MPa ($\sigma_{11} = -45$ MPa), $\sigma_2 = -47$ MPa ($\sigma_{22} = -66$ MPa), $\sigma_3 = -199$
 18 MPa ($\sigma_{33} = -108$ MPa).

1 Another problem arises when only 3 directions are used in stress analysis, there is no way to
2 estimate the errors for the stress components. It is better to use a least-squares solution of
3 equation (5) (respectively (4) for full stress tensor) which can be obtained when more than 3
4 (respectively 6 for full stress tensor) lattice strain measurements are performed. For example,
5 at $z = 1.73$ mm (E0F2), although the {10.3} diffraction peaks are extremely well defined and
6 thus their location accurately established, the relative difference of the principal components
7 varies from 45 % to 165 % with the normal component values of the full stress tensor (Table
8 1). When the 3 reflections are simultaneously taken into account (resolving 9 measurement
9 directions instead of 3), the large uncertainties given by the least-squares method allow for the
10 solving quality of the equation system to be appraised (Table 1) and enable thus the detection
11 of anomalies in the stress analysis. At $z = 8.27$ mm (E2F2, Table 1), the situation is in stark
12 contrast to the previous one, with a low uncertainty. This allows us to conclude that the
13 stresses, calculated by fitting the experimental data to equation (5), are a relevant analysis of
14 the true state of strain/stress. It should be recalled that the calculated stress values obtained
15 with equation (4) ($\sigma_1 = 51$ MPa, $\sigma_2 = -72$ MPa, $\sigma_3 = -110$ MPa) are close to the normal stress
16 components determined by equation (5). As explained above, the true principal stress values
17 are different ($\sigma_1 = 27$ MPa, $\sigma_2 = -47$ MPa, $\sigma_3 = -199$ MPa) because a large deviation of the
18 principal stress directions from the sample axes is observed (Table 2).

19 3.4 Influence of second-order stresses on residual stress analysis in LPBF produced Ti- 20 6Al-4V part

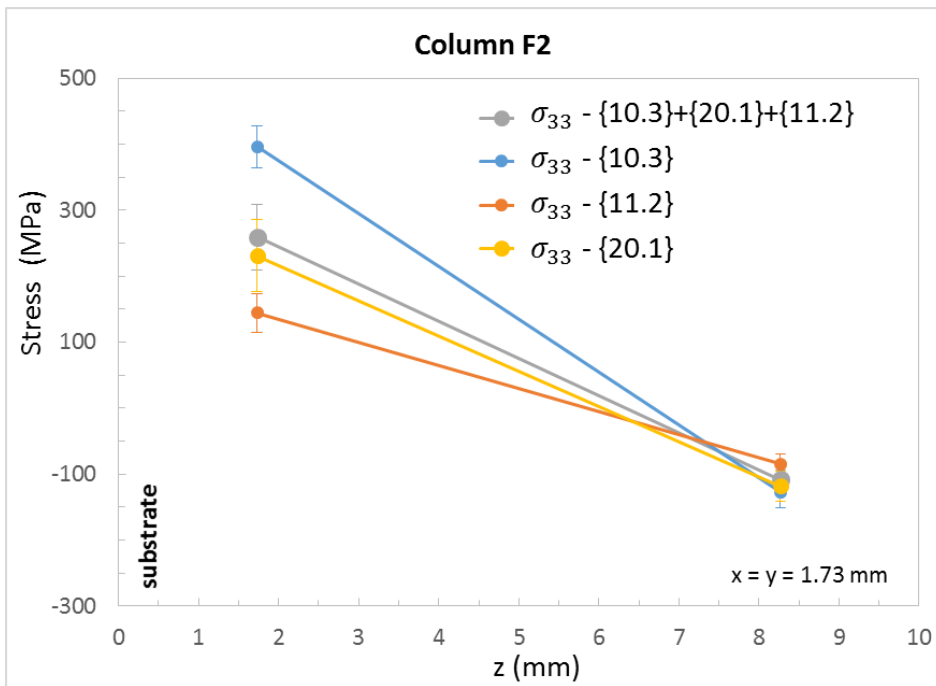
21 The full stress tensor has been determined with the relation (4) where the second-order
22 stresses (or intergranular stresses) are neglected. In this case, the deviations of grain
23 (mesoscopic) stresses from macroscopic stresses are hence considered to be solely due to
24 elastic anisotropy. Residual stresses are also generated by inhomogeneous thermo-elastic or
25 plastic deformations on two scales: one length scale is given by the size of the studied sample;

1 the size of the grains forming the polycrystal defines the second one. The first-order (or
2 macroscopic) stresses are given by the inhomogeneity on the part length scale. The second-
3 order (or intergranular) stresses are given by the inhomogeneity on the grain size scale
4 (mesoscopic scale). Both are superimposed and a combination of first- and second-order
5 stresses is given by ND measurements. Concerning the LPBF process, three origins of
6 residual stresses can stand: difference in plastic flow caused by undergone stress, phase
7 transformation or non-uniform shrinkage during cooling. If we have a superposition of both
8 macroscopic and important intergranular contributions, the presence of intergranular strain
9 influences the measured elastic strain. The stress values calculated by equation (4) will then
10 necessarily vary with the $\{hk.l\}$ reflection [30,40]. In most studies, stress analysis by XRD or
11 ND is only performed with a single reflection. The importance of second-order stresses can
12 thus never be quantified or even identified. To ascertain this, the evolution of the residual
13 stresses for each of the 3 analyzed plane families $\{10.3\}$, $\{20.1\}$ and $\{11.2\}$ alone are shown
14 in Figure 5, and compared with the results obtained previously when the 3 reflections are
15 simultaneously used for the complete stress analysis. For the sake of clarity, only σ_{33}
16 evolution is shown for the columns F0 (Figure 5.a) and F2 (Figure 5.b).



1
2

(a)



3
4

(b)

5 Figure 5: stress distribution determined with the relation (4) using a single (either {10.3} or
6 {11.2} or {20.1}) or multiple ({10.3}+{11.2}+{20.1}) {hk.l} reflections for stress analysis
7 along F0 (a) and F2 (b) columns.

1 The stress values change strongly from one reflection to another. For example, for the central
2 column F0 at $z = 8.27$ mm, $\sigma_{33}(hk.l)$ values reach -230 ± 31 MPa for $\{20.1\}$ and -84 ± 24
3 MPa for $\{11.2\}$. On the other hand, at $z = 1.73$ mm, the stress values for the different
4 reflections are similar, with values ranging from -475 ± 20 MPa to -516 ± 70 MPa. An
5 opposite trend is observed for the column F2: at $z = 1.73$ mm, σ_{33} values significantly differ
6 ($\sigma_{33}(10.3) = 396 \pm 32$ MPa and $\sigma_{33}(11.2) = 144 \pm 30$ MPa) while, at $z = 8.27$ mm, closer
7 stress values are determined by ND. It should be noted that this phenomenon is not due to a
8 limited set of measurement directions (10 (φ, ψ) directions per reflection in the present case).
9 The uncertainties obtained for each reflection are similar to those determined for the full
10 stress tensor. The fitting of the data to equation (4) seems to be proper as revealed by the low
11 level of the estimated uncertainties. The results obtained previously, when the 3 reflections
12 are used simultaneously, logically show intermediate values (Figure 5). The calculated stress
13 clearly depends on the analyzed plane family. This reflection dependence of the stress values
14 obtained by ND clearly indicates that strain incompatibilities are present at the grain scale.
15 The diffracting grains are not the same for each $\{hk.l\}$ reflection and this allows us to deduce
16 that different second-order stresses exist, related to a strong thermic and/or plastic anisotropic
17 deformation for this set of grains. High temperature gradients, as a result of the locally
18 concentrated energy input, lead to high stress gradients. A residual stress gradient between
19 core regions and the surface of the part is present. Its magnitude depends on the part
20 geometry, the material stiffness and the temperature fields. As a consequence, the
21 development of stress is locally affected and depends on the location in the sample. The
22 development of second-order stresses is strongly dependent on the thermal history of the
23 probed region. However, the results obtained with several $\{hk.l\}$ reflections provide valuable
24 information on the residual stress generation and should reduce the effects of second-order
25 stresses on the macroscopic stress evaluation due to its averaging effect.

4. Conclusions

In this present work, the residual stress distribution in a Ti-6Al-4V sample, produced by means of LPBF technology, has been evaluated using ND. Residual stress development in LPBF parts is mostly caused by large cooling rates and high-temperature gradient, proper to the process. The bottom and top surfaces of LPBF specimens tend to be in tension or low compression while the internal volume stands in compression. Residual stress in the LPBF part could be reduced and homogenized through the optimization of process parameters (e.g., preheating, scanning strategy). A relevant mapping of the stress values through the full depth of AM parts has to consider the full stress tensor consisting of 6 stress components, otherwise determined stress values might be distorted or even wrong, mistaking between compression and tension stress state. Furthermore, in LPBF process, non-negligible residual second-order stress gradients arise from the different interdependent physical phenomena (metallurgical, thermal, mechanical and fluid mechanic aspects) occurring during this highly non-equilibrium process for hexagonal alloys which are generally highly anisotropic materials. These stresses can be detected by ND with the use of multiple $\{hk.l\}$ reflections. To obtain a relevant stress analysis, a large number of (φ, ψ) directions (i.e. more than 6 lattice strain measurements) is required to minimize the effects of a single erroneous reflection profile measurement and to enable an assessment of the quality of the least-squares fitting to the experimental data.

Acknowledgments

This work is based upon experiments performed at the STRESS-SPEC instrument operated by FRMII at the Heinz Maier-Leibnitz Zentrum (MLZ), Garching, Germany. The authors thank the MLZ neutron Facilities scientific comities for the allocated experimental days (experiment 11962).

1 This study is part of the FATAL project managed by IRT Jules Verne (French Institute in
2 Research and Technology in Advanced Manufacturing). The authors wish to associate the
3 industrial and academic partners of this project; respectively, ACB, Arts et Métiers ParisTech,
4 CNRS, DAHER, Ecole Centrale de Nantes, Europe Technologies, FIVES, Renault and
5 University of Nantes.

6

1 REFERENCES

- 2 [1] E. William Frazier: *J. Mater. Eng. Perform.*, 2014, vol. 23, pp. 1917-1928.
- 3 [2] C. Y. Yap, C. K. Chua¹, Z. L. Dong, Z. H. Liu, D. Q. Zhang, L. E. Loh, S. L. Sing:
4 *Appl. Phys. Rev.*, 2015, vol. 2, pp. 1-21.
- 5 [3] L.-C. Zhang, H. Attar: *Adv. Eng. Mater.*, 2016, vol. 18, pp. 463-475.
- 6 [4] W.S.W. Harun, N.S. Manam, M.S.I.N. Kamariah, S. Sharif, A.H. Zulkifly, I. Ahmad,
7 H. Miura: *Powder Technol.*, 2018, vol. 331, pp. 74-97.
- 8 [5] J.-P. Kruth, L. Froyen, J. Van Vaerenbergh, P. Mercelis, M. Rombouts, B. Lauwers: *J.*
9 *Mater. Process. Tech.*, 2004, vol. 149, pp. 616-622.
- 10 [6] D.W. Brown, J.D. Bernardin, J.S. Carpenter, B. Clausen, D. Spornjak, J.M.
11 Thompson: *Mater. Sci. Eng. A*, 2016, vol. 678, pp. 291–298.
- 12 [7] M. Awd, J. Tenkamp, M. Hirtler, S. Siddique, M. Bambach, F. Walther: *Materials*,
13 2018, vol. 11, pp. 1-17.
- 14 [8] Bey Vrancken: Study of residual stresses in selective laser melting, Faculty of
15 engineering Science, PhD dissertation, University of Leuven, 2016.
- 16 [9] P. Mercelis, J.-P. Kruth: *Rapid Prototyping J.*, 2006, vol. 12, pp. 254–265.
- 17 [10] H. Shipley, D. McDonnell, M. Culleton, R. Coull, R. Lupoi, G. O'Donnell, D.
18 Trimble: *Int. J. Mach. Tool. Manu.*, 2018, vol. 128, pp. 1–20.
- 19 [11] M. B. Prime: *J. Eng. Mater. Tech.*, 2000, vol. 123, pp. 162-168.
- 20 [12] ASTM Standard E837 REV A: Standard Test Method for Determining Residual
21 Stresses by the Hole-Drilling Strain-Gage Method, ASTM International, West Conshohocken,
22 PA, 2013.

- 1 [13] M.B. Prime: Appl. Mech. Rev., 1999, vol. 52, pp. 75-96.
- 2 [14] Y. Liu, Y. Yang, D. Wang: Int. J. Adv. Manuf. Tech., 2016, vol. 87, pp. 647–656.
- 3 [15] L.S. Anderson, A.M. Venter, B. Vrancken, D. Marais, J. Van Humbeeck, T.H. Becker:
4 Mater. Res. Proc., 2018, vol. 4, pp. 73-78.
- 5 [16] V. Hauk, Structural and Residual Stress Analysis by Nondestructive Methods,
6 Elsevier, Amsterdam, 1997.
- 7 [17] D. Gloaguen, G. Oum, V. Legrand, J. Fajoui, S. Branchu: Acta Mater., 2013, vol. 61,
8 pp. 5779-5790.
- 9 [18] L. Pintschovius, V. Jung, E. Macherauch, O. Vohringer: Mater. Sci. Eng., 1983, vol.
10 61, pp. 43-50.
- 11 [19] L. Steven Anderson, Evaluating measurement techniques: establishing a testing
12 framework for residual stress in selective laser melted Ti-6Al-4V, faculty of Engineering PhD
13 dissertation, University of Stellenbosch, 2017.
- 14 [20] A. Kromm, S. Cabeza, T. Mishurova, N. Nadammal, T. Thiede, G. Bruno: Mater. Res.
15 Proc., 2018, vol. 6, pp. 259-264.
- 16 [21] V.-D. Le, E. Pessard, F. Morel, F. Edy: Eng. Fract. Mech., 2019, vol. 214, pp. 410-
17 426.
- 18 [22] B. B. He, Two-dimensional X-ray Diffraction, John Wiley & Sons, 2018, pp.292-293.
- 19 [23] P. J. Withers, M. Preuss, A. Steuwer, J. W. L. Pang: J. Appl. Cryst., 2007, vol. 40, pp.
20 891-904.
- 21 [24] H. Dölle, V. Hauk: Z. Metalkde, 1978, vol. 69, pp. 410-417.
- 22 [25] A. Baczmanski, N. Hfaiedh, M. François, K. Wierzbanowski: Mater. Sci. Eng. A,
23 2009, vol. 501, pp. 153-165.

- 1 [26] I.C. Noyan: Mater. Sci. Eng., 1985, vol. 75, pp. 95-103.
- 2 [27] M. Hofmann, W. Gan, J. Rebelo-Kornmeier: Journal of large-scale research facilities,
3 2015, vol. 1 A6, pp.1-4.
- 4 [28] J. Rebelo Kornmeier, M. Hofmann, W.M. Gan, C. Randau, K. Braun, K. Zeitelhack, I.
5 Defendi, J. Krueger, E. Faulhaber, H. Brokmeier: Mater. Sci. Forum, 2017, vol. 905, pp.
6 151-156.
- 7 [29] G. Simmons, H. Wang: Single crystal elastic constants and calculated aggregate
8 properties, M.I.T. Press, Cambridge M.A., 1971.
- 9 [30] D. Gloaguen, T. Berchi, E. Girard, R. Guillén: J. Nucl. Mater., 2008, vol. 374, pp.
10 138-146.
- 11 [31] U.F. Kocks, C.N. Tomé and H.R. Wenk: texture and anisotropy, Cambridge university
12 press, 1998, pp.288-289.
- 13 [32] P. Mercelis, J.-P. Kruth: Rapid Prototyping J., 2006, vol. 12, pp. 254–265.
- 14 [33] T. Simson, A. Emmel, A. Dwars, J. Böhm: Addit. Manuf., 2017, vol. 17, pp. 183–189.
- 15 [34] C. Li, Z.Y. Liu, X.Y. Fang, Y.B. Guo: Procedia CIRP, 2018, vol. 71, pp. 348-353.
- 16 [35] H. Ali, L. Ma, H. Ghadbeigi, K. Mumtaz: Mater. Sci. Eng. A, 2017, vol. 695, pp. 211-
17 220.
- 18 [36] R. Mertens, B. Vrancken, N. Holmstock, Y. Kinds, J.-P. Kruth, J. Van Humbeeck:
19 Physics Procedia, 2016, vol. 83, pp. 882-890.
- 20 [37] I. Yadroitec, I. Yadroitsava: Virtual Phys. Prototyp., 2015, vol. 10, pp. 67–76.
- 21 [38] M.E. Fitzpatrick, A. Lodini: Analysis of Residual Stress by Diffraction using Neutron
22 and Synchrotron radiation, Taylor & Francis, 2003.

- 1 [39] R.A Winholtz, A.D. Krawitz: Mater. Sci. Eng. A, 1996, vol. 205, pp. 257-258.
- 2 [40] D. Gloaguen, M. François, R. Guillén: J. Appl. Cryst., 2004, vol. 37, pp. 934-940.
- 3

1 **Figures captions:**

2 Figure 1: schematic of the sample with measurement positions (in green) taken in the analysis
3 Note the coordinate system (x,y,z) where the x and y directions are parallel to the baseplate
4 and the z direction is the part building direction.

5
6 Figure 2: neutron diffraction patterns of the Ti-6Al-4V sample for different (φ, ψ) directions
7 for the E1F0 measurements position. The diffraction peaks used in the study are also given.

8
9 Figure 3: residual stresses obtained by neutron diffraction at several build heights in the
10 central column F0 (a and b) and the column F2 (c and d) close to a corner of the analyzed
11 cube.

12
13 Figure 4: residual stresses obtained by neutron diffraction at several building levels: close
14 substrate (E1: a and b) and close surface (E2: c and d).

15
16 Figure 5: stress distribution determined with the relation (4) using a single (either {10.3} or
17 {11.2} or {20.1}) or multiple ({10.3}+{11.2}+{20.1}) {hk.l} reflections for stress analysis
18 along F0 (a) and F2 (b) columns.

19

1 **Tables captions:**

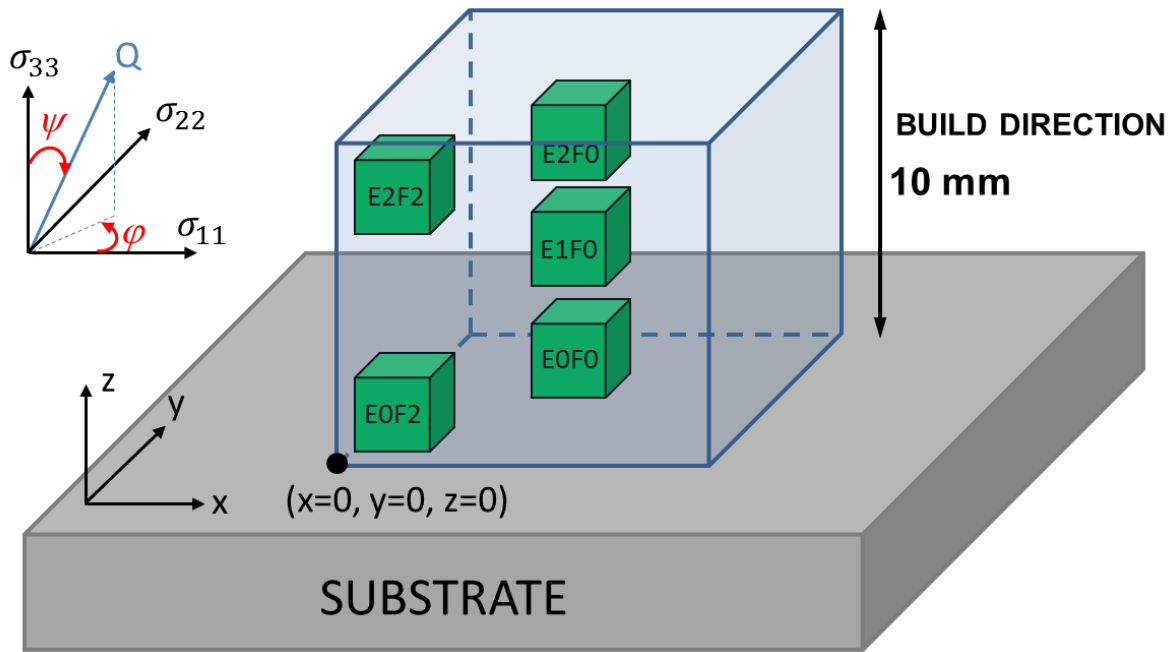
2 Table 1: evolution of the principal stress components σ_i , calculated from equation (5), for
3 different {hk.l} reflections and compared to the results obtained for the normal components
4 σ_{ii} , obtained with the relation (4), along the column F2.

5 Table 2: angles between the principal stress directions (X,Y,Z) and the specimen orthogonal
6 stress directions (x,y,z) for the different measurement positions.

7

8

1



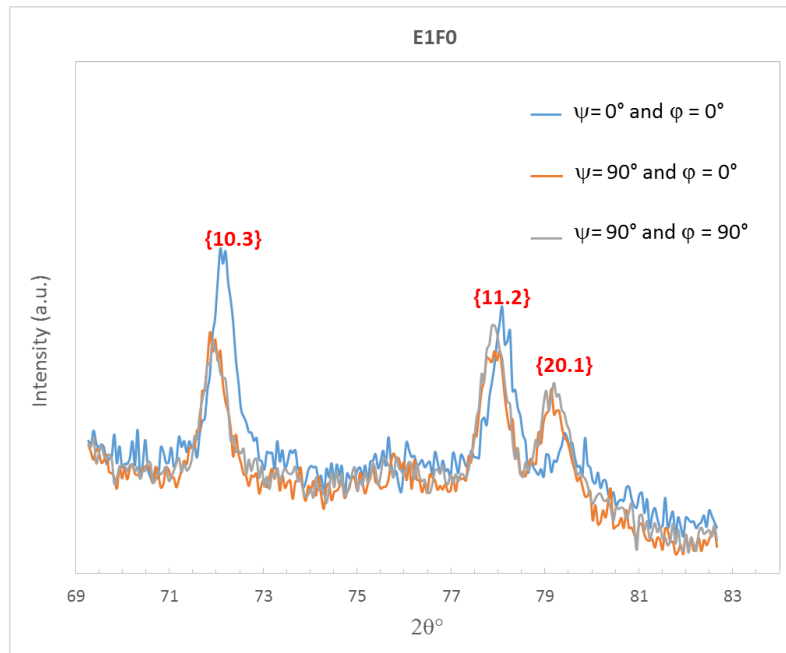
2

3 Figure 1: schematic of the sample with measurement positions (in green) taken in the analysis

4 Note the coordinate system (x,y,z) where the x and y directions are parallel to the baseplate

5 and the z direction is the part building direction.

6

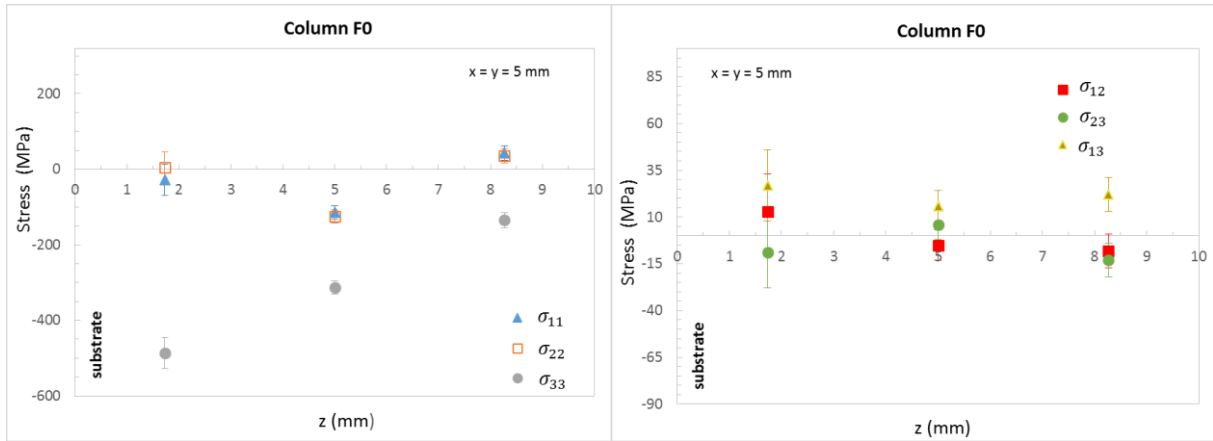


1

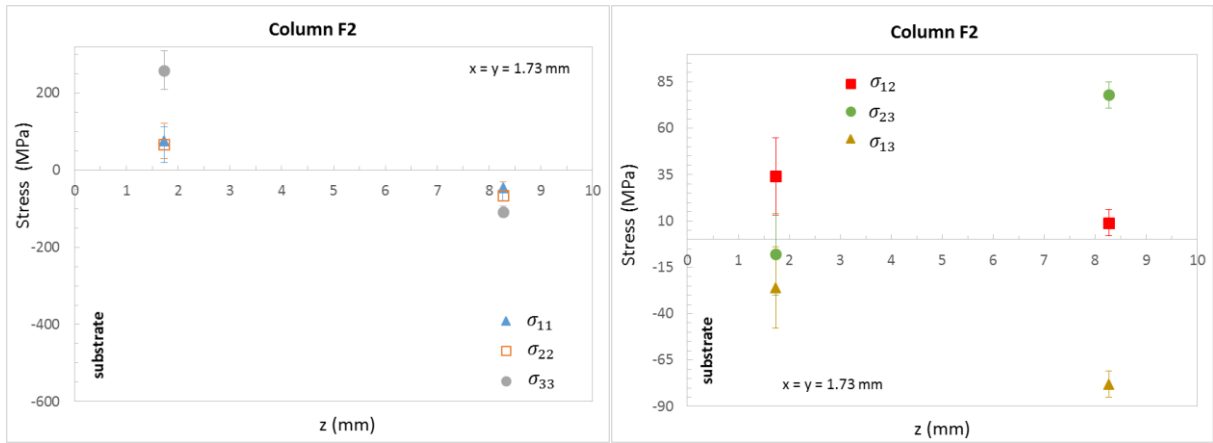
2 Figure 2: neutron diffraction patterns of the Ti-6Al-4V sample for different (ϕ, ψ) directions
3 for the E1F0 measurements position. The diffraction peaks used in the study are also given.

4

5



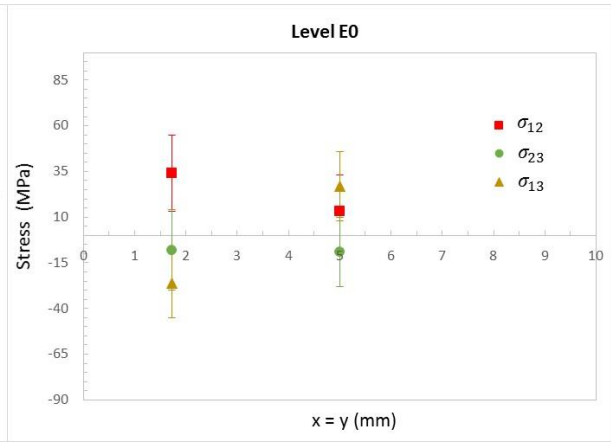
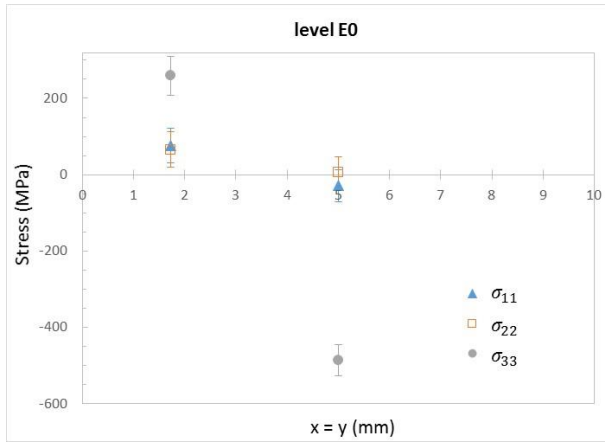
1
2
3



4
5

6 Figure 3: residual stresses obtained by ND at several building heights in the central column
 7 F0, i.e. core sample (a and b) and the column F2 (c and d) close to a corner of the analyzed
 8 cube.

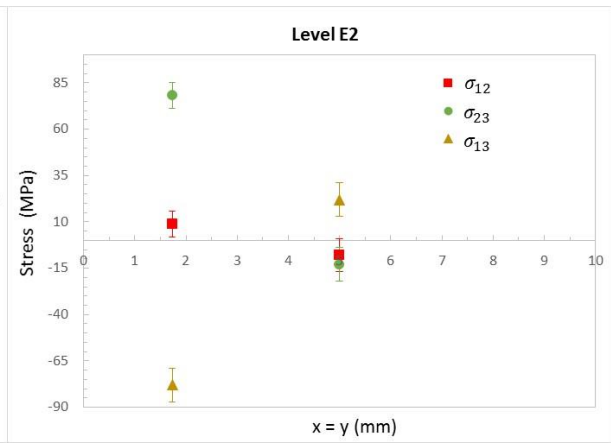
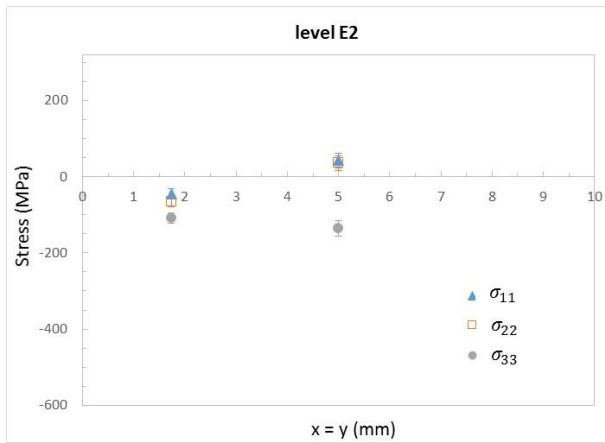
9



1

2 (a)

(b)



3

4 (c)

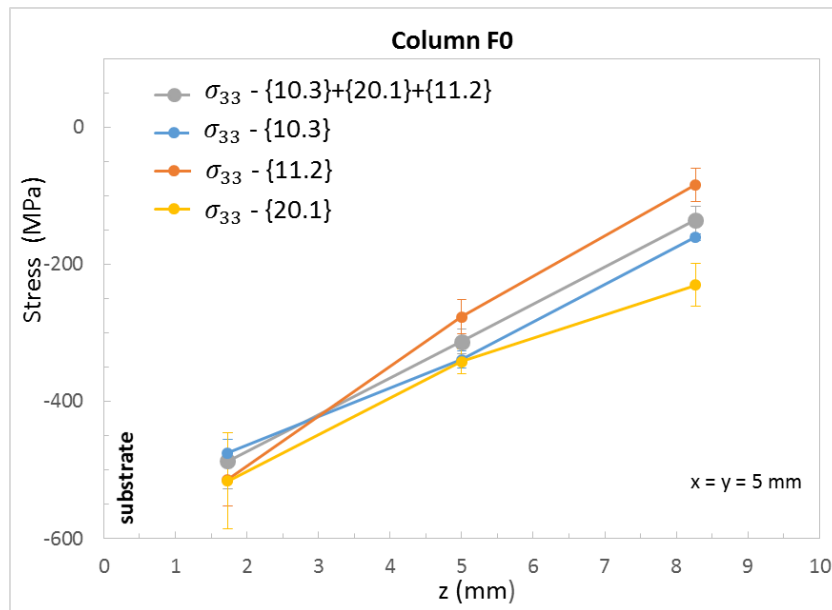
(d)

5 Figure 4: residual stresses obtained by neutron diffraction at several building levels: close
 6 substrate (E1: a and b) and close surface (E2: c and d).

7

1

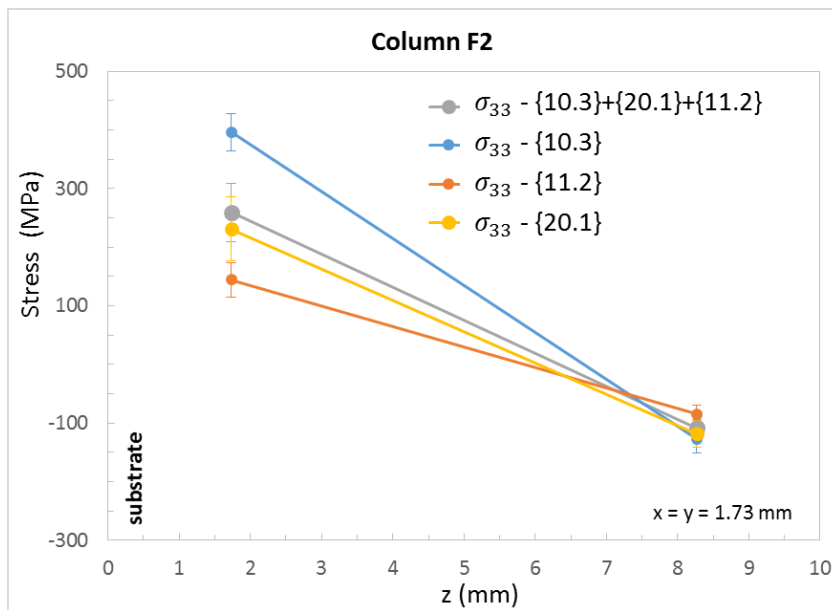
2



3

4

(a)



5

6

(b)

7 Figure 5: stress distribution determined with the relation (4) using a single (either {10.3} or
 8 {11.2} or {20.1}) or multiple ({10.3}+{11.2}+{20.1}) {hk.l} reflections for stress analysis
 9 along F0 (a) and F2 (b) columns.

10

Stress component	Assumption	E0F2	E2F2
σ_1 (MPa)	Principal stress- $\{10.3\}$	202	-46
	Principal stress- $\{11.2\}$	27	-37
	Principal stress- $\{20.1\}$	-291	-69
	Principal stress $\{10.3\}+\{21.1\}+\{20.1\}$	-16 ± 135	-51 ± 16
	σ_{11} -full stress tensor	76 ± 46	-45 ± 14
σ_2 (MPa)	Principal stress- $\{10.3\}$	166	-74
	Principal stress- $\{11.2\}$	18	-51
	Principal stress- $\{20.1\}$	-277	-91
	Principal stress $\{10.3\}+\{21.1\}+\{20.1\}$	-25 ± 135	-72 ± 16
	σ_{22} -full stress tensor	66 ± 46	-66 ± 14
σ_3 (MPa)	Principal stress- $\{10.3\}$	376	-137
	Principal stress- $\{11.2\}$	166	-84
	Principal stress- $\{20.1\}$	-354	-112
	Principal stress $\{10.3\}+\{21.1\}+\{20.1\}$	62 ± 135	-110 ± 16
	σ_{33} -full stress tensor	259 ± 50	-108 ± 14

1 Table 1: evolution of the principal stress components σ_i , calculated from equation (5), for
2 different $\{hk.l\}$ reflections and compared to the results obtained for the normal components
3 σ_{ii} , obtained with the relation (4), along the column F2.

4

Measurement position	Angle between x and X (in degree)	Angle between y and Y (in degree)	Angle between z and Z (in degree)
E0F0	19°	19°	4°
E0F2	137°	41°	9°
E1F0	19°	18°	5°
E2F0	34°	33°	8°
E2F2	51°	42°	40°

- 1 Table 2: angles between the principal stress directions (X,Y,Z) and the specimen orthogonal
- 2 stress directions (x,y,z) for the different measurement positions.